Electronic Supplementary Material (ESI) for Chemical Science.

Tuning Symmetry and Magnetic Blocking of an Exchange-Coupled Lanthanide Ion in Isomeric, Tetrametallic Complexes: $[LnCl_6(TiCp_2)_3]$

Ningxin Jiang,[1] Daria Nakritskaia,[2] Jiaze Xie,[3] Arun Ramanathan,[1] Sergey Varganov,[2] Henry S. La Pierre[1,4]*

1 School of Chemistry and Biochemistry, Georgia Institute of Technology, Atlanta, Georgia 30332-0400, United States.

2 Department of Chemistry, University of Nevada, Reno, Nevada 89557-0216, United States;

3 Department of Chemistry, University of Chicago, Chicago, Illinois 60637, United States

4 Nuclear and Radiological Engineering and Medical Physics Program, School of Mechanical Engineering, Georgia Institute of Technology, Atlanta, Georgia 30332-0400, United States.

Table of Contents

1. General Considerations

Unless otherwise stated, all reagents were obtained from commercial suppliers, and the syntheses and manipulations were conducted under argon with exclusion of dioxygen (O_2) and H_2O using Schlenk techniques or in an inert atmosphere box (Vigor) under a dinitrogen (<0.1 ppm of O_2/H_2O) atmosphere. The glovebox is equipped with two −35 °C freezers. All glassware were stored in an oven overnight (>8 h) at a temperature of ca. 160 °C prior to use. Celite and molecular sieves were dried under vacuum at a temperature >250 °C for a minimum of 24 h. Diethyl ether, n-hexane, benzene, toluene, and tetrahydrofuran (THF) were purged with UHP-grade argon (Airgas) and passed through columns containing Q-5 and molecular sieves in a solvent purification system (JC Meyer Solvent Systems). All solvents in the glovebox were stored in bottles over 3 Å molecular sieves. The reagent $(Cp_2TiCl)_2$ ($Cp = C_5H_5^-$) was prepared by published procedures.[1] Elemental analyses were determined at University of California, Berkeley, Microanalytical Facility (Berkeley, CA). All four samples do not give resolvable proton or carbon NMR spectra.

2. Synthetic Procedures

$[(C_5H_5)_2TiCl]_3TbCl_3$ (pseudo-octahedral geometry, O-Tb). Inside a glovebox, 4 mL of toluene was added to a 20 mL scintillation vial charged with anhydrous $TbCl_3$ (0.122 g, 0.460 mmol), $(Cp_2TiCl)_2$ (0.300 g, 0.702 mmol), and a Teflon stir bar. The reaction mixture was stirred overnight and a green solid precipitated from the olive mixture. The precipitant was filtered off through a fine porosity frit with minimal additional toluene. The solid on the frit was dried *in vacuo* to afford the title compound as teal powder in 82% yield (0.340 g). X-ray diffraction (XRD) quality crystals were grown from the diffusion of hexane into a solution of **O-Tb** in toluene at room temperature. All the spectroscopy, magnetic property measurements, and elemental analysis were performed on the XRD quality crystals (The crystals are ground for magnetic property and infrared (IR) measurements). The IR spectrum of **O-Tb** is shown in Fig. S7a. The Raman spectroscopy of **O-Tb** is shown in Fig. S7b. Elemental analysis found (calculated) for: C 39.85(39.78), H 3.34(3.34).

$[(C_5H_5)_2TiCl]_3TbCl_3$ (trigonal prismatic geometry, TP-Tb). Inside a glovebox, 3 mL of THF was added to a 20 mL scintillation vial charged with anhydrous $TbCl_3$ (0.080 g, 0.302 mmol) and a Teflon stir bar. The reaction mixture was allowed to stir overnight at room temperature and dried *in vacuo* to afford $TbCl_3{\cdot}xTHF$. $(Cp_2TiCl)_2$ (0.060 g, 0.140 mmol) and 2 mL of toluene was added to the same vial with $TbCl_3{\cdot}xTHF$. The reaction mixture was stirred overnight at 308 K and filtered through a pipet packed with glass filter paper and Celite. Hexane was allowed to diffuse into the filtrate and single-crystals of **TP-Tb** and **O-Tb** were observed on the wall of vials. The mother liquor was decanted, and all of the single crystals were covered with Paratone oil and transferred outside the glovebox. The **TP-Tb** single crystals were separated from the **O-Tb** and **TP-Tb** mixture by using a Mitogen loop under an optical microscope under the protection of Paratone oil on a glass slide. The **TP-Tb** crystalized in a needle shape, while the **O-Tb** crystalized into the parallelepiped shape. The unit cells determined by the diffractometer are used to confirm the phase of separated **TP-Tb**. Each reaction produces less than 0.5 mg **TP-Tb** crystals. The separated **TP-Tb** was transferred back into the glove box and the Paratone oil are removed by washing with hexane. All the spectroscopy, magnetic property measurements and elemental analysis were performed on the XRD quality crystals (The crystals are ground for magnetic property and IR measurements). The infrared spectrum of of **TP-Tb** is shown in Fig. S7a. The Raman spectrum of **TP-Tb** is shown in Fig. S7b. Elemental analysis found (calculated) for: C 39.74(39.78), H 3.35(3.34).

$[(C_5H_5)_2TiCl]_3GdCl_3$ (trigonal prismatic geometry, TP-Gd). Inside a glovebox, 3 mL of THF was added to a 20 mL scintillation vials charged with anhydrous $GdCl_3$ (0.121 g, 0.460 mmol) and a Teflon stir bar. The reaction mixture was allowed to stir overnight at room temperature and reduced *in vacuo* to afford the $GdCl_3{\cdot}xTHF$. $(Cp_2TiCl)_2$ (0.300 g, 0.702 mmol) and 4 mL of toluene was added to the same vial with $GdCl_3{\cdot}xTHF$. The reaction mixture was again stirred overnight and a green solid precipitated from the olive-colored mixture. The precipitant was filtered off on a fine porosity frit with minimal additional toluene. The solid on the frit was dried *in vacuo* to afford the **TP-Gd** complex as green powder in 57% yield (0.235 g). X-ray diffraction (XRD) quality crystals were grown from the diffusion of hexane into a solution of **TP-Gd** in toluene at room temperature. All the spectroscopy, magnetic property measurements and elemental analysis were performed on the XRD quality crystals (The crystals were ground for magnetic property and IR measurements). The infrared spectrum (IR) of **TP-Gd** is shown in Fig. S7a. The Raman

spectrum of **TP-Gd** is shown in Fig. S7b. Elemental analysis found (calculated) for: C 39.82(39.95), H 3.25(3.34).

$[(C_5H_5)_2TiCl]_3GdCl_3$ (octahedral geometry, O-Gd). Inside a glovebox, 2 mL of diethyl ether was added to a 20 mL scintillation vial charged with Gd powder (0.200 g, 1.27 mmol), Cp_2TiCl_2 (0.040 g, 0.161 mmol), and a Teflon stir bar. The reaction mixture was stirred overnight at room temperature and the color of the reaction changed from orange to green. The reaction mixture was dried under *vacuo*. 1 mL of toluene was added into the dried mixture. After shaking the mixture for 2 minutes, the mixture was filtered through pipet packed with glass filter paper and Celite. The hexane was allowed to diffuse into the filtrate and single-crystals of **TP-Gd** and **O-Gd** were crystalized. All the single crystals are covered with Paratone oil and transferred outside the glovebox after the removal of mother liquor. The **O-Gd** single crystals were separated from the **O-Gd** and **TP-Gd** mixture by using a Mitogen loop under an optical microscope under the protection of Paratone oil on a glass slide. The **TP-Gd** crystalized in needle shape while the **O-Gd** crystalized into the parallelepiped shape. The unit cells determined by diffractometer are used to confirm the phase of separated **O-Gd**. Each reaction produces less than 0.2 mg **O-Gd** crystals. The separated **O-Gd** was transferred back into the glove box and the Paratone oil are removed by hexane. All the spectroscopy were performed on the XRD quality crystals (The crystals are ground for IR measurements). The infrared spectroscopy (IR) of **O-Gd** is shown in Fig. S7a. The Raman spectroscopy of **O-Gd** is shown in Fig. S7b. The elemental analysis and magnetic properties measurements are not performed on **O-Gd** due to the limited yield of the reaction.

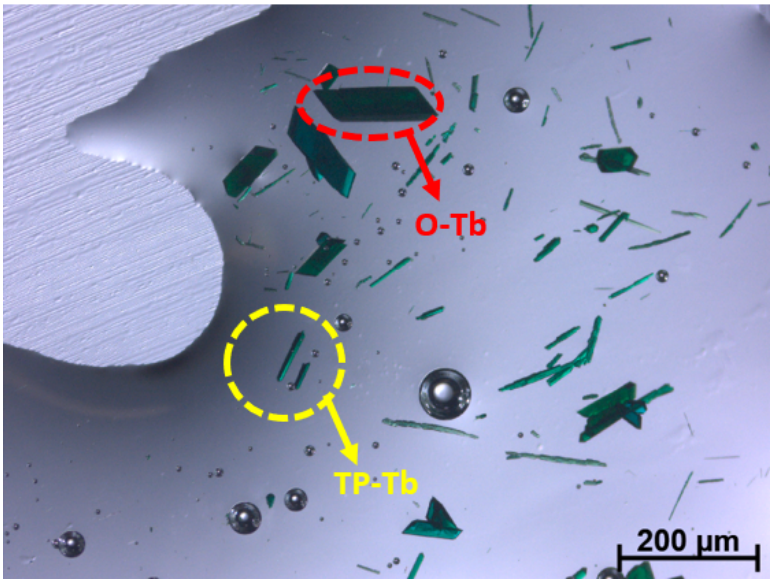

Figure S1. Crystals of **O-Tb** and **TP-Tb** that crystalized from the filtrate of reaction between $(Cp_2TiCl)_2$ and excess $TbCl_3$ in toluene. The picture was acquired with a ZEISS Stereo microscope (Stemi 508) and a ZEISS Axiocam ERc 5s microscope camera.

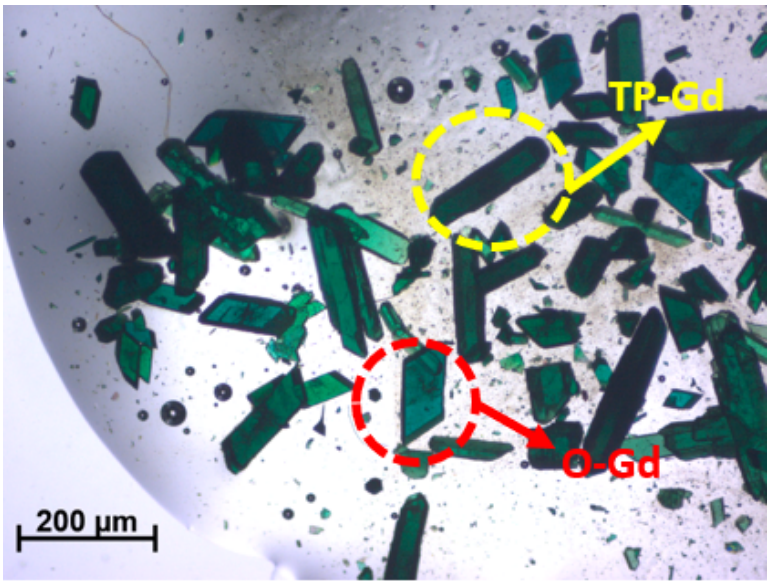

Figure S2. Crystals of **O-Gd** and **TP-Gd** that crystalized from the toluene solution of product from the reaction between Cp_2TiCl_2 and excess Gd powder in diethyl ether. The picture was acquired with a ZEISS Stereo microscope (Stemi 508) and a ZEISS Axiocam ERc 5s microscope camera.

3. Crystallographic data and analysis

Crystals suitable for X-ray diffraction were covered in Paratone oil in a glovebox and transferred to the diffractometer in a 20 mL capped vial. Crystals were mounted on a loop with Paratone oil on a Bruker D8 VENTURE diffractometer. The crystals were cooled and kept at T = 100 K during data collections (The XRD data of **TP-Tb** and **TP-Gd** were collected at both 100 K and 300 K). The structures were solved with the ShelXT structure solution program using the Intrinsic Phasing solution method and by using Olex2 as the graphical interface.[2] The model was refined with version 2014/7 of XL by using least-squares minimization.[3] The SHAPE program was used for the geometry analysis and the result is shown in Table S9 and S10.[4-6]

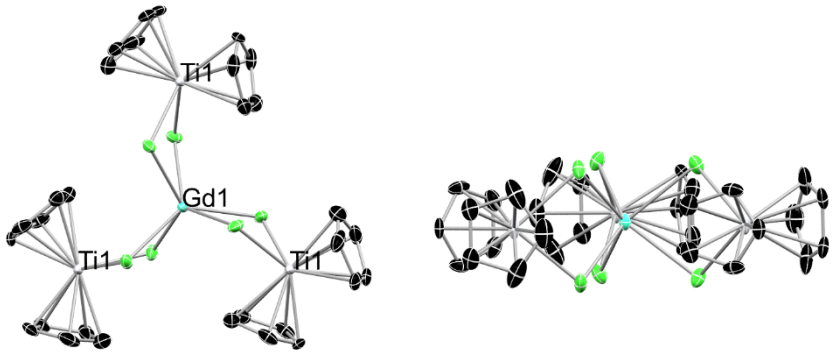

$[(C_5H_5)_2TiCl]_3GdCl_3$
TP-Gd

Figure S3. Molecular structure of **TP-Gd** at 100 K. Thermal ellipsoids are shown at 50% probability and H atoms are omitted for clarity. Black, blue, green, and grey represent carbon, gadolinium, chlorine, and titanium, respectively.

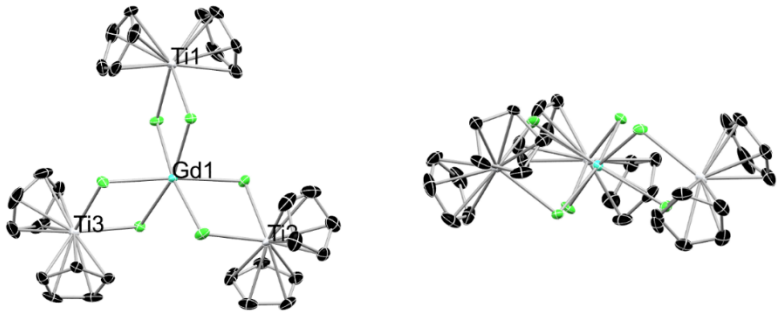

$[(C_5H_5)_2TiCl]_3GdCl_3$
O-Gd

Figure S4. Molecular structure of **O-Gd** at 100 K. Thermal ellipsoids are shown at 50% probability and H atoms are omitted for clarity. Black, blue, green, and grey represent carbon, gadolinium, chlorine, and titanium, respectively.

Table S1. Crystallographic data for **TP-Tb**, **O-Tb**, **TP-Gd**, and **O-Gd** at 100 K.

Compound	**TP-Tb**	**O-Tb**	**TP-Gd**	**O-Gd**
Empirical formula	$C_{30}H_{30}Cl_6TbTi_3$	$C_{30}H_{30}Cl_6TbTi_3$	$C_{30}H_{30}Cl_6GdTi_3$	$C_{30}H_{30}Cl_6GdTi_3$
Formula weight	905.86	905.86	904.19	904.19
Temperature / K	100	100	100.0	100.0
Crystal system	hexagonal	monoclinic	hexagonal	monoclinic
Space group	$P6_3/m$	$P2_1/n$	$P6_3/m$	$P2_1/n$
a / Å	12.7237(4)	12.7966(8)	12.7286(4)	12.7944(3)
b / Å	12.7237(4)	21.4650(13)	12.7286(4)	21.4986(5)
c / Å	11.3427(5)	12.9750(7)	11.3424(5)	12.9783(3)
α / °	90	90	90	90
β / °	90	114.419(2)	90	114.4540(10)
γ / °	120	90	120	90
Volume / $Å^3$	1590.28(12)	3245.2(3)	1591.46(12)	3249.60(13)
Z	2	4	2	4
ρ_{calc} / $g \cdot cm^{-3}$	1.892	1.854	1.887	1.848
μ / mm^{-1}	3.447	3.379	3.307	3.239
F(000)	886.0	1772.0	884.0	1768.0
Crystal size / mm^3	0.566 × 0.192 × 0.106	0.387 × 0.286 × 0.156	0.566 × 0.192 × 0.106	0.302 × 0.264 × 0.214
Radiation	MoKα (λ = 0.71073 Å)	MoKα (λ = 0.71073 Å)	MoKα (λ = 0.71073 Å)	MoKα (λ = 0.71073 Å)
2θ range for data collection/°	6.404 to 61.042	3.936 to 61.09	5.154 to 61.02	3.934 to 54.968
Index ranges	-17 ≤ h ≤ 18, -17 ≤ k ≤ 18, -16 ≤ l ≤ 16	-15 ≤ h ≤ 18, -25 ≤ k ≤ 30, -18 ≤ l ≤ 18	-18 ≤ h ≤ 18, -18 ≤ k ≤ 18, -16 ≤ l ≤ 16	-16 ≤ h ≤ 16, -24 ≤ k ≤ 27, -16 ≤ l ≤ 13
Reflections collected	17260	38624	29818	39063
Independent reflections	1697 [R_{int} = 0.0496, R_{sigma} = 0.0226]	9885 [R_{int} = 0.0572, R_{sigma} = 0.0487]	1703 [R_{int} = 0.0529, R_{sigma} = 0.0186]	7401 [R_{int} = 0.0367, R_{sigma} = 0.0236]
Data/restraints/parameters	1697/42/84	9885/0/361	1703/42/84	7401/16/377
Goodness-of-fit on F^2	1.042	1.052	1.037	1.117

Final R indexes [I>=2σ (I)]	R_1 = 0.0311, wR_2 = 0.0776	R_1 = 0.0360, wR_2 = 0.0929	R_1 = 0.0305, wR_2 = 0.0735	R_1 = 0.0232, wR_2 = 0.0584
Final R indexes [all data]	R_1 = 0.0317, wR_2 = 0.0782	R_1 = 0.0384, wR_2 = 0.0950	R_1 = 0.0326, wR_2 = 0.0742	R_1 = 0.0234, wR_2 = 0.0586
Largest diff. peak/hole ($e \cdot Å^{-3}$)	1.50/-0.8	1.36/-1.05	1.59/-0.81	0.55/-0.81
Completeness to 2θ	99.5%	99.8%	99.7%	99.6%

Table S2. Crystallographic data for **TP-Gd** and **TP-Tb** at 300 K.

Compound	**TP-Gd**	**TP-Tb**
Empirical formula	$C_{30}H_{30}Cl_6GdTi_3$	$C_{30}H_{30}Cl_6TbTi_3$
Formula weight	904.19	905.86
Temperature / K	300.0	300
Crystal system	hexagonal	hexagonal
Space group	$P6_3/m$	$P6_3/m$
a / Å	12.8073(11)	12.8107(18)
b / Å	12.8073(11)	12.8107(18)
c / Å	11.5663(14)	11.571(2)
α / °	90	90
β / °	90	90
γ / °	120	120
Volume / $Å^3$	1643.0(3)	1644.6(6)
Z	2	2
ρ_{calc} / $g \cdot cm^{-3}$	1.828	1.829
μ / mm^{-1}	3.203	3.334
F(000)	884.0	886
Crystal size / mm^3	0.364 × 0.125 × 0.028	0.308 × 0.225 × 0.109
Radiation	MoK*α* (λ = 0.71073)	MoKα (λ = 0.71073)
2θ range for data collection/°	5.088 to 56.534	5.086 to 61.036
Index ranges	-17 ≤ h ≤ 17, -16 ≤ k ≤ 17, -15 ≤ l ≤ 15	-17 ≤ h ≤ 18, -18 ≤ k ≤ 18, -16 ≤ l ≤ 16

Reflections collected	11333	21314
Independent reflections	1421 [R_{int} = 0.0530, R_{sigma} = 0.0280]	1757 [Rint = 0.0702, Rsigma = 0.0303]
Data/restraints/parameters	1421/42/84	1757/39/75
Goodness-of-fit on F^2	1.140	1.103
Final R indexes [I>=2σ (I)]	R_1 = 0.0356, wR_2 = 0.0827	R1 = 0.0338, wR2 = 0.0830
Final R indexes [all data]	R_1 = 0.0425, wR_2 = 0.0889	R1 = 0.0413, wR2 = 0.0900
Largest diff. peak/hole (e·Å^{-3})	0.81/-1.05	0.69/-1.49
Completeness to 2θ	99.8%	99.8%

* The 300 K SCXRD data of **TP-Gd** and **TP-Tb** was collected since the simulated PXRD patterns of **TP-Gd** and **TP-Tb** from SCXRD result at 100 K does not match well (peak position shifts can be observed) with the experimental PXRD patterns measured at 300 K which suggests that there is a unit cell volume change with changed temperature. The 300 K SCXRD result shows a bigger unit cell compared to the 100 K result which indicates the positive thermal expansion in **TP-Gd** and **TP-Tb** and the simulated PXRD patterns from the 300 K structure match well with the experimental PXRD patterns collected at room temperature as shown in Fig. S5b and Fig. S5c.

Table S3: Fractional Atomic Coordinates (×10^4) and Equivalent Isotropic Displacement Parameters (Å^2×10^3) for **TP-Tb** at 100 K. U_{eq} is defined as 1/3 of the trace of the orthogonalised U_{ij}.

Atom	*x*	*y*	*z*	*U*(eq)
Tb1	3333.33	6666.67	7500	14.35(9)
Cl1	2852.4(6)	4829.6(6)	6049.4(6)	21.01(14)
Ti1	3508.4(6)	3709.2(6)	7500	18.14(15)
C1A	5458(5)	5342(5)	6902(6)	31.2(9)
C2A	5321(4)	4215(5)	6511(4)	26.5(8)
C3A	5268(6)	3582(6)	7500	22.2(10)
C4A	2800(3)	1675(3)	6869(4)	28.7(8)
C5A	1955(4)	2007(3)	6491(5)	44.8(12)
C6A	1457(6)	2223(6)	7500	43.9(16)
C1B	5336(8)	3839(7)	6905(9)	31.2(9)
C2B	5425(7)	4949(7)	6515(5)	26.5(8)
C3B	5426(9)	5554(8)	7500	22.2(10)
C4B	1500(30)	2210(20)	6940(30)	28.7(8)
C5B	2320(30)	1850(30)	6518(14)	44.8(12)
C6B	2880(40)	1690(50)	7500	43.9(16)

Table S4: Fractional Atomic Coordinates (×10^4) and Equivalent Isotropic Displacement Parameters (Å^2×10^3) for **TP-Tb** at 300 K. U_{eq} is defined as 1/3 of the trace of the orthogonalised U_{ij}.

Atom	*x*	*y*	*z*	*U*(eq)
Tb1	3333.33	6666.67	7500	28.83(11)
Ti1	6277.1(6)	6476.6(6)	7500	32.17(17)
Cl1	5151.6(7)	7116.2(7)	6075.4(6)	38.14(18)
C4	8303(4)	7198(4)	6905(5)	73.5(13)
C5	7974(4)	8009(6)	6526(6)	94.3(19)
C6	7770(6)	8513(6)	7500	87(2)
C1A	4436(9)	4563(10)	7500	42.2(17)
C2A	5079(8)	4574(8)	6528(5)	46.5(15)
C3A	6135(8)	4634(8)	6901(9)	53.2(14)
C1B	6428(8)	4748(8)	7500	42.2(17)
C2B	5760(7)	4683(6)	6527(4)	46.5(15)
C3B	4671(7)	4542(6)	6903(7)	53.2(14)

Table S5: Fractional Atomic Coordinates ($\times 10^4$) and Equivalent Isotropic Displacement Parameters ($Å^2 \times 10^3$) for **O-Tb** at 100 K. U_{eq} is defined as 1/3 of the trace of the orthogonalised U_{ij}.

Atom	*x*	*y*	*z*	*U*(eq)
Tb1	4486.4(2)	2713.4(2)	3510.0(2)	13.93(5)
Ti1	4017.1(4)	2397.7(2)	6283.8(4)	14.32(9)
Ti3	5162.6(4)	1263.3(2)	2023.7(4)	14.81(9)
Ti2	4026.1(4)	4428.2(2)	2281.3(4)	17.64(9)
Cl2	2846.0(5)	2816.5(3)	4262.0(5)	16.62(11)
Cl4	3454.5(6)	3309.2(3)	1577.3(5)	18.78(12)
Cl6	3540.0(6)	1654.6(3)	2534.9(6)	19.66(12)
Cl3	5315.5(6)	3857.9(3)	4138.9(6)	21.20(12)
Cl1	5572.4(6)	2230.2(3)	5544.3(6)	20.83(13)
Cl5	6108.0(6)	2319.5(3)	2896.6(5)	17.01(12)
C7	5482(2)	3098.6(13)	7440(2)	19.1(5)
C8	4996(3)	2840.1(15)	8132(2)	23.6(6)
C6	4630(3)	3443.2(13)	6571(2)	21.8(5)
C10	3612(3)	3406.4(15)	6750(3)	29.7(7)
C9	3840(3)	3037.6(17)	7706(3)	30.4(7)
C25	5368(3)	1680.9(15)	431(2)	26.2(6)
C1	2819(4)	1517.5(14)	5412(3)	35.9(8)
C11	2638(3)	4371.4(17)	3032(4)	39.5(9)
C16	4829(3)	5257.6(13)	1650(3)	26.1(6)
C29	6475(4)	954.8(15)	3880(3)	36.6(8)
C5	2501(3)	1769.2(15)	6240(4)	38.4(8)
C21	4293(3)	1872.2(17)	375(2)	32.6(7)
C2	3931(4)	1294.9(14)	5963(4)	39.5(9)
C30	5443(3)	672.4(18)	3684(3)	37.2(8)
C4	3407(4)	1683.7(17)	7280(3)	40.7(9)
C24	5355(3)	1034.7(16)	309(3)	31.2(7)
C22	3609(3)	1317(2)	201(3)	41.5(9)
C3	4292(4)	1406.9(16)	7116(3)	42.9(10)

Atom	*x*	*y*	*z*	*U*(eq)
C26	5176(3)	265.4(17)	2799(3)	39.2(8)
C27	6048(4)	276.2(15)	2432(3)	39.0(9)
C15	2045(3)	4444(2)	1858(4)	40.1(9)
C17	4254(3)	4872.0(16)	708(3)	34.6(7)
C23	4277(4)	816.6(19)	174(3)	38.6(8)
C20	5726(3)	4923.4(18)	2450(3)	36.9(8)
C12	3266(3)	4941(3)	3429(4)	57.2(15)
C28	6866(3)	717.3(17)	3080(3)	37.4(8)
C13	3014(4)	5311.8(17)	2496(6)	68.6(19)
C18	4822(5)	4299.5(17)	914(4)	51.2(12)
C19	5723(4)	4323.9(19)	1990(5)	54.3(13)
C14	2303(4)	5007(3)	1569(5)	61.3(16)

Table S6: Fractional Atomic Coordinates ($\times 10^4$) and Equivalent Isotropic Displacement Parameters ($Å^2 \times 10^3$) for **TP-Gd** at 100 K. U_{eq} is defined as 1/3 of the trace of the orthogonalised U_{ij}.

Atom	*x*	*y*	*z*	*U*(eq)
Gd1	3333.33	6666.67	7500	16.98(9)
Cl1	2842.4(6)	4811.8(6)	6047.6(6)	24.08(14)
Ti1	3504.9(5)	3699.8(6)	7500	20.72(15)
C1A	5449(4)	5332(5)	6895(5)	31.8(9)
C2A	5315(4)	4217(5)	6505(4)	28.5(8)
C3A	5268(6)	3584(5)	7500	23.3(10)
C4A	2808(3)	1669(3)	6867(4)	29.7(8)
C5A	1956(4)	1996(3)	6489(5)	47.0(12)
C6A	1458(6)	2205(6)	7500	46.0(16)
C1B	5339(7)	3841(7)	6904(9)	31.8(9)
C2B	5420(7)	4935(7)	6510(5)	28.5(8)
C3B	5418(9)	5542(8)	7500	23.3(10)
C4B	1490(20)	2190(20)	6920(20)	29.7(8)
C5B	2320(20)	1850(20)	6507(12)	47.0(12)
C6B	2850(30)	1640(40)	7500	46.0(16)

Table S7: Fractional Atomic Coordinates ($\times 10^4$) and Equivalent Isotropic Displacement Parameters ($Å^2 \times 10^3$) for **TP-Gd** at 300 K. U_{eq} is defined as 1/3 of the trace of the orthogonalised U_{ij}.

Atom	*x*	*y*	*z*	*U*(eq)
Gd1	6666.67	3333.33	2500	29.39(14)
Cl1	7123.7(9)	5167.4(9)	3928.2(8)	38.2(2)
Ti1	6479.7(8)	6285.4(8)	2500	32.1(2)
C1A	4730(10)	6410(10)	2500	36.8(18)
C2A	4673(7)	5751(8)	1516(6)	42.2(17)
C3A	4544(8)	4670(8)	1887(9)	47.8(16)
C4A	7187(6)	8309(6)	3121(6)	47.0(16)

Atom	*x*	*y*	*z*	*U*(eq)
C5A	8028(8)	7978(7)	3502(7)	64(2)
C6A	8508(10)	7778(11)	2500	62(3)
C1B	4568(11)	4452(11)	2500	36.8(18)
C2B	4589(9)	5100(9)	1523(7)	42.2(17)
C3B	4654(9)	6155(9)	1887(10)	47.8(16)
C4B	8465(18)	7797(16)	3088(17)	47.0(16)
C5B	7609(19)	8100(20)	3489(11)	64(2)
C6B	7150(30)	8340(30)	2500	62(3)

Table S8: Fractional Atomic Coordinates ($\times 10^4$) and Equivalent Isotropic Displacement Parameters ($Å^2 \times 10^3$) for **O-Gd** at 100 K. U_{eq} is defined as 1/3 of the trace of the orthogonalised U_{ij}.

Atom *x*	*y*	*z*	*U*(eq)
Gd1	5504.2(2)	7287.7(2)	6479.2(2)	12.81(4)
Ti1	4831.4(3)	8743.3(2)	7967.3(3)	13.31(8)
Ti2	5967.3(3)	5570.2(2)	7713.6(4)	16.28(8)
Ti3	5975.4(3)	7601.9(2)	3700.0(3)	13.10(8)
Cl1	6458.5(4)	8349.3(2)	7464.7(5)	18.32(10)
Cl2	3875.1(4)	7691.3(2)	7090.0(4)	15.66(10)
Cl3	6534.0(4)	6686.6(2)	8422.1(4)	17.6(1)
Cl4	4674.5(4)	6137.3(2)	5853.1(5)	20.08(11)
Cl5	7154.7(4)	7187.1(2)	5723.3(4)	15.3(1)
Cl6	4416.2(5)	7773.1(3)	4431.5(5)	19.69(11)
C1	3945(3)	9727.4(12)	7561(2)	35.2(6)
C2	3125(2)	9285.7(14)	6901(3)	33.8(6)
C3	3526(3)	9052.8(12)	6111(2)	33.1(6)
C4	4552(3)	9335.8(14)	6309(2)	33.8(6)
C5	4834(3)	9737.7(14)	7202(3)	35.3(6)
C6	4627(2)	8965.4(13)	9677(2)	28.0(5)
C7	4629(2)	8320.9(12)	9560.6(19)	24.0(5)
C8	5708(2)	8138.6(14)	9619(2)	30.9(6)
C9	6383(2)	8690.2(17)	9797(2)	38.1(7)
C10	5703(3)	9190.3(15)	9818(2)	35.6(6)
C21	7180(3)	8481.2(12)	4566(2)	35.0(7)
C22	7497(2)	8229.0(13)	3742(3)	36.6(7)
C23	6575(3)	8311.4(14)	2699(2)	40.5(8)
C24	5691(3)	8591.0(14)	2867(3)	41.2(8)
C25	6068(3)	8703.4(12)	4018(3)	38.2(7)
C26	6382(2)	6594.7(13)	3238(2)	29.8(6)
C27	6158(2)	6960.4(13)	2281(2)	29.1(6)
C28	4999(2)	7153.2(12)	1857.1(19)	22.0(5)
C29	4508.4(18)	6899.9(10)	2547.9(18)	16.6(4)
C30	5368(2)	6556.9(11)	3418.5(19)	20.4(4)
C11	4263(3)	5671.9(15)	7997(4)	51.1(10)
C12	4267(2)	5071.9(14)	7539(3)	34.7(6)
C13	5176(2)	4740.0(11)	8350(2)	24.4(5)
C14	5735(3)	5129.6(14)	9285(2)	32.8(6)

Atom	*x*	*y*	*z*	*U*(eq)
C15	5157(4)	5698.3(14)	9070(4)	50.4(10)
C16A	7281(12)	5613(5)	6911(6)	27.8(14)
C17A	6722(7)	5023(4)	6622(6)	29.7(18)
C18A	7030(6)	4687(2)	7610(9)	30.0(16)
C19A	7747(6)	5040(3)	8513(5)	29.3(14)
C20A	7953(6)	5606(3)	8107(5)	24.6(9)
C16B	7500(20)	5674(8)	7083(11)	27.8(14)
C17B	6774(14)	5192(8)	6404(7)	29.7(18)
C18B	6812(11)	4708(5)	7117(13)	30.0(16)
C19B	7552(12)	4856(5)	8210(10)	29.3(14)
C20B	7956(11)	5459(5)	8228(9)	24.6(9)

Table S9. Structural deviations of **TP-Tb** and **TP-Gd** from various six-coordinate geometries determined by SHAPE calculation.

TP-Tb		**TP-Gd**	
Structure	Deviation	Structure	Deviation
Hexagon (D_{6h})	22.771	Hexagon (D_{6h})	22.713
Pentagonal pyramid (C_{5v})	14.541	Pentagonal pyramid (C_{5v})	14.542
Octahedron (O_h)	20.146	Octahedron (O_h)	20.256
Trigonal prism (D_{3h})	**4.428**	**Trigonal prism (D_{3h})**	**4.505**
Johnson Pentagonal Pyramid J2 (C_{5v})	16.354	Johnson Pentagonal Pyramid J2 (C_{5v})	16.302

Table S10. Structural deviations of **O-Tb** and **O-Gd** from various six-coordinate geometries determined by SHAPE calculation.

O-Tb		**O-Gd**	
Structure	Deviation	Structure	Deviation
Hexagon (D_{6h})	23.979	Hexagon (D_{6h})	23.979
Pentagonal pyramid (C_{5v})	23.633	Pentagonal pyramid (C_{5v})	23.633
Octahedron (O_h)	**8.277**	**Octahedron (O_h)**	**8.277**
Trigonal prism (D_{3h})	13.803	Trigonal prism (D_{3h})	13.803
Johnson Pentagonal Pyramid J2 (C_{5v})	24.056	Johnson Pentagonal Pyramid J2 (C_{5v})	24.056

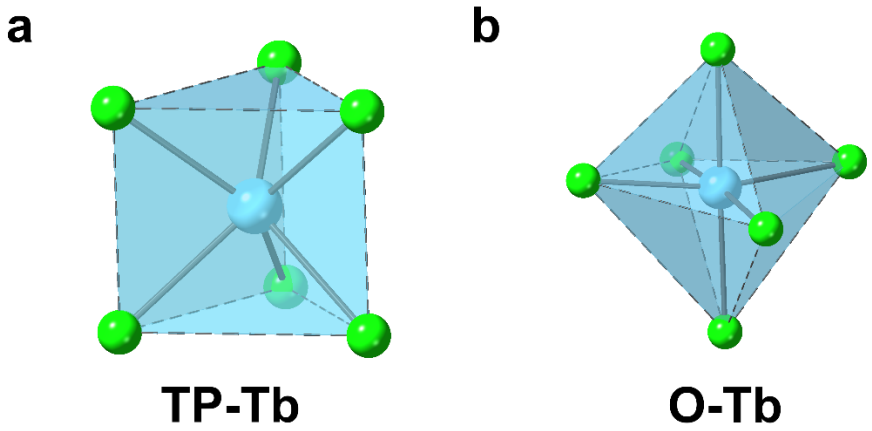

Figure S5. Demonstration of $(TbCl_6)^{3-}$ polyhedra in (a) **TP-Tb** and (b) **O-Tb**. The carbon, hydrogen and titanium atoms are omitted for clarity. Blue and green represent terbium and chlorine, respectively.

4. Phase purity study

Laboratory PXRD data were collected on a PANalytical X'Pert PRO Alpha-1 diffractometer with a Cu K*α* source. The sample was loaded and sealed in a domed sample holder inside the glovebox.

Infrared (IR) samples were taken on a Bruker ALPHA FTIR spectrometer from 400 to 4000 cm^{-1}. IR samples were prepared as Nujol mulls sandwiched between two KBr plates.

Raman spectroscopy measurement was conducted on a Renishaw Raman Spectrometer using 20x objective lens with the excitation of a 488 nm laser. The scattered light was dispersed using a holographic notch filter with a grating of 1200 lines/mm. The Raman spectrum was recorded from 112.4 to 3210 cm^{-1} by setting the center position at 1800 cm^{-1} with an acquisition time of 60 seconds for each spectrum. The single crystal sample was placed inside an NMR tube and the tube was sealed with a cap and taped with parafilm to prevent the inclusion of air.

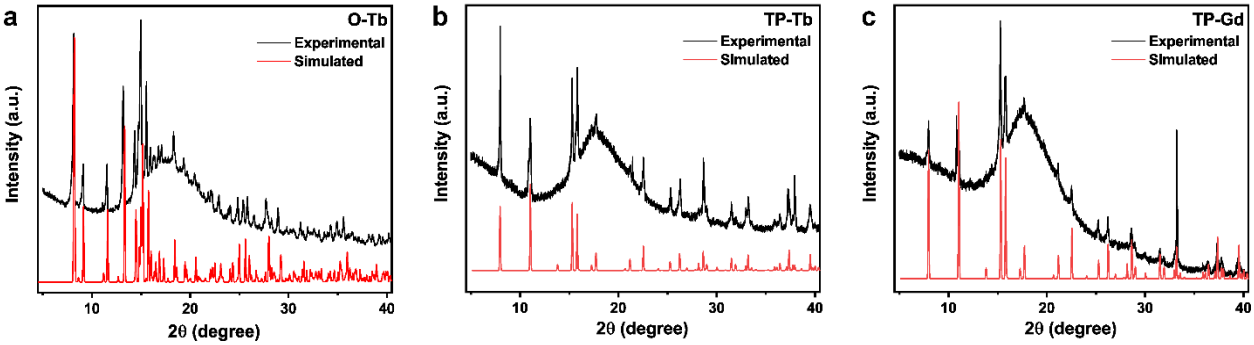

Figure S6. (a) Experimental, and simulated PXRD patterns (based on SCXRD structure under 100 K) of **O-Tb**. (b) Experimental, and simulated PXRD patterns (based on SCXRD structure under 300 K) of **TP-Tb**. (c) Experimental, and simulated PXRD patterns (based on SCXRD structure under 300 K) of **TP-Gd**. (The broad contributions centered at 18 degree are from the domed sample holder which prevent the oxidation of samples.)

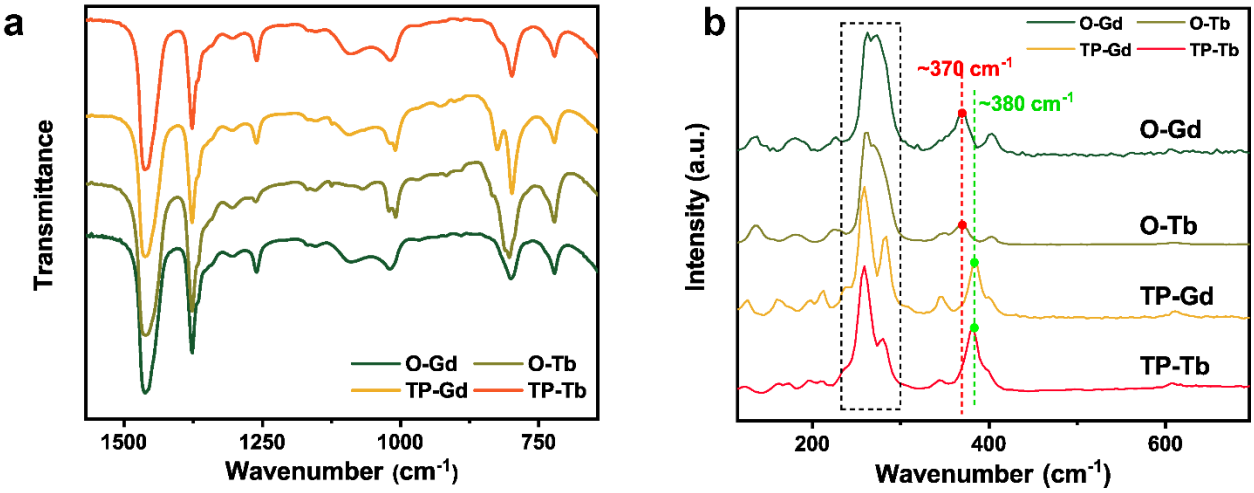

Figure S7. (a) IR spectra of **TP-Tb**, **O-Tb**, **TP-Gd**, and **O-Gd** on powder samples (b) Raman spectra of **TP-Tb**, **O-Tb**, **TP-Gd**, and **O-Gd** on single crystal samples.

To confirm the phase purity of compounds, the powder X-ray diffraction (PXRD) measurement (Fig. S5) was performed on **O-Tb**, **TP-Tb**, and **TP-Gd**. The PXRD was not performed on **O-Gd** due to their limited reaction yield. The PXRD patterns for **O-Tb**, **TP-Tb**, and **TP-Gd** match well with the simulated patterns from SCXRD results which suggests the phase purity of these two samples. Although the IR spectra of four samples are similar (Fig. S6a), notable difference can be observed in the Raman spectra for **TP-Ln** and **O-Ln** (Fig. S6b). From 330 cm^{-1} to 450 cm^{-1}, only peaks centered at 370 cm^{-1} and 400 cm^{-1} are observed for **O-Ln**, while for **TP-Gd** and **TP-Tb**, peaks centered at 350 cm^{-1} and 380 cm^{-1} are found. The peaks from 350 to 400 cm^{-1} could be assigned to the symmetrical stretching vibration of Ln-Cl bonds.[7] In addition, two peaks can be found in **TP-Ln** from 230 cm^{-1} to 320 cm^{-1}, while one peak with a shoulder peak are observed in **O-Ln**. It is noteworthy that the Raman measurements were conducted on single crystal level and cannot reflect the bulk phase purity of samples. To confirm the reproducibility for the synthesis of **TP-Tb**, the magnetic measurement was conducted twice on **TP-Tb** and two measurement results show good agreements (Fig. S7)

5. Magnetic properties

All the magnetic measurements were performed on a Quantum Design MPMS with powder samples in polycarbonate capsules. The power samples were suspended in an eicosane matrix to prevent movement and protect the sample from incidental air exposure. Diamagnetic corrections for the capsule and eicosane were made by measuring temperature vs moment in triplicate for each to determine a moment per gram correction. Pascal's constants were used to correct for the diamagnetic contribution from the complexes.[8]

The software PHI was used to fit the dc magnetic susceptibility data for **TP-Gd**.[9] The spin-only Hamiltonian $\widehat{H} = -3J_{Ti-Gd}\hat{S}_{Ti}\hat{S}_{Gd} - 3J_{Ti-Ti}\hat{S}_{Ti}\hat{S}_{Ti}$ was used. Both the temperature dependence magnetic susceptibility data from 2 K to 300 K and the magnetic field dependence magnetization data at 2 K, 3 K, 4 K and 5 K were used for the fit. Contributions for temperature-independent paramagnetism (TIP) and intermolecular coupling (zJ') were included when fitting the susceptibility data.

Magnetic properties of TP-Tb

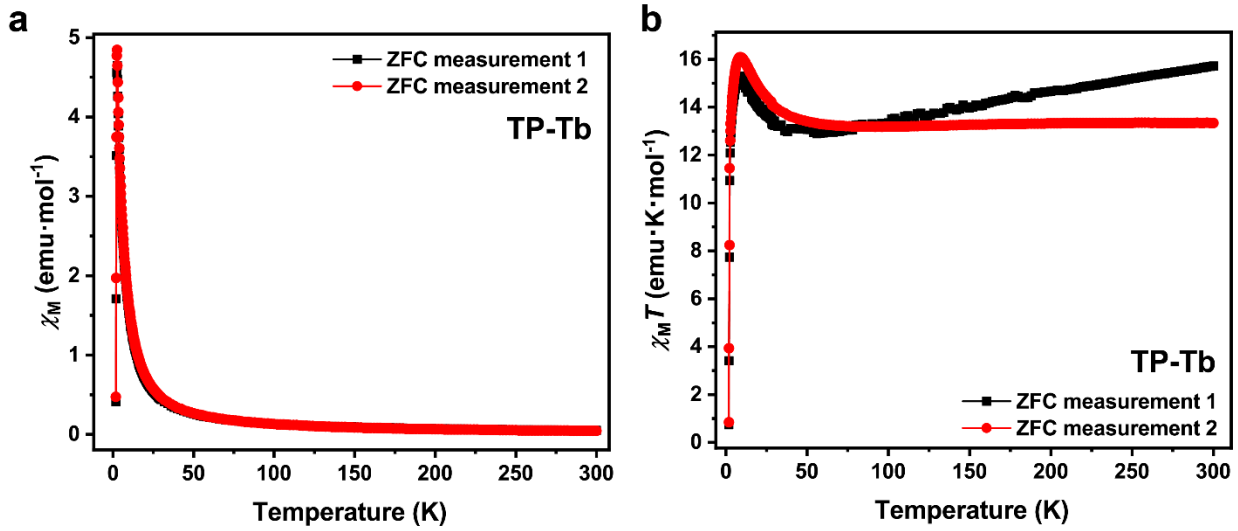

Figure S8. Temperature dependence of (a) χ_M and (b) $\chi_M T$ under 0.1 T dc magnetic field from 2 K to 300 K for **TP-Tb**. The measurement 1 and measurement 2 are performed on two different batches of samples (measurement 1: 4 mg, measurement 2: 8.3 mg.) The lines are shown to guide the eye.

The good match of between the dc magnetic measurement results at low temperature from two different batches of sample suggests the good reproducibility of the physical separation methods for preparing **TP-Tb**. The increasing $\chi_M T$ value of **TP-Tb** from 100 K to 300 K in measurement 1 can be attributed to the existence of different amount of remaining temperature independent term, χ_0. (The temperature independent term from eicosane has been subtracted from the raw data).

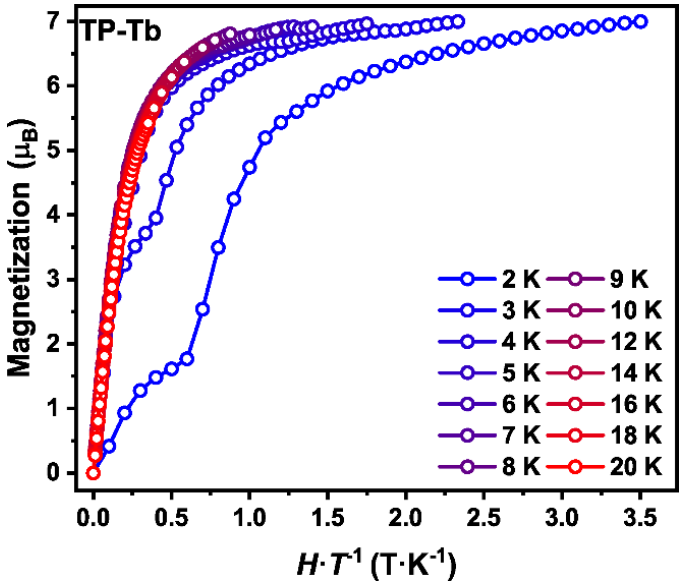

Figure S9. H/T dependence of magnetization for **TP-Tb** from 2 K to 20 K. The lines are shown to guide the eye.

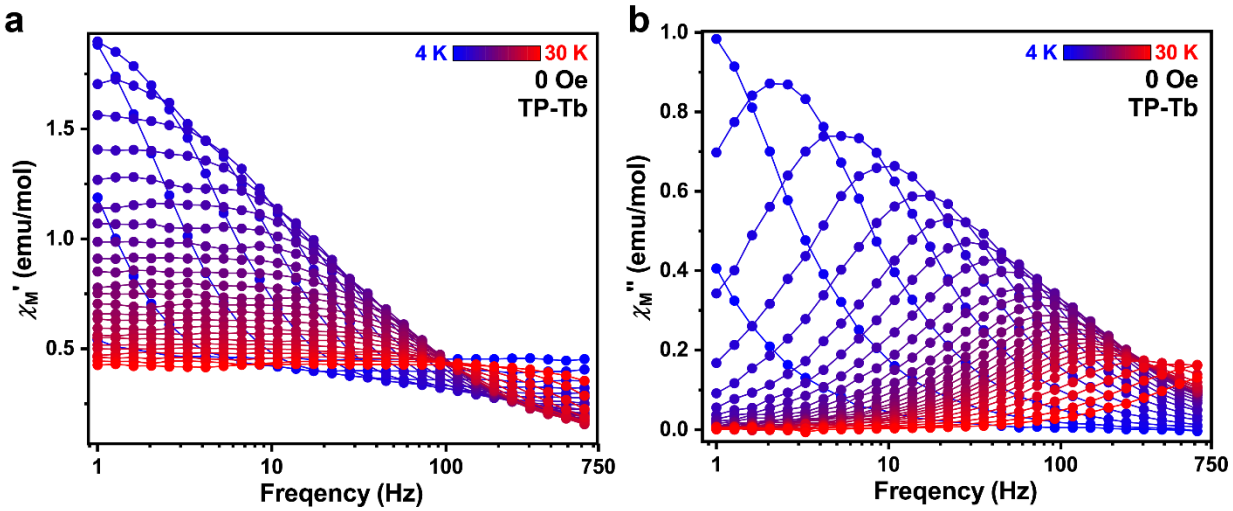

Figure S10. (a) Frequency dependence of χ_M' under zero dc magnetic field from 4 K to 30 K for **TP-Tb**. (b) Frequency dependence of χ_M'' under zero dc magnetic field from 4 K to 30 K for **TP-Tb**. The lines are shown to guide the eye.

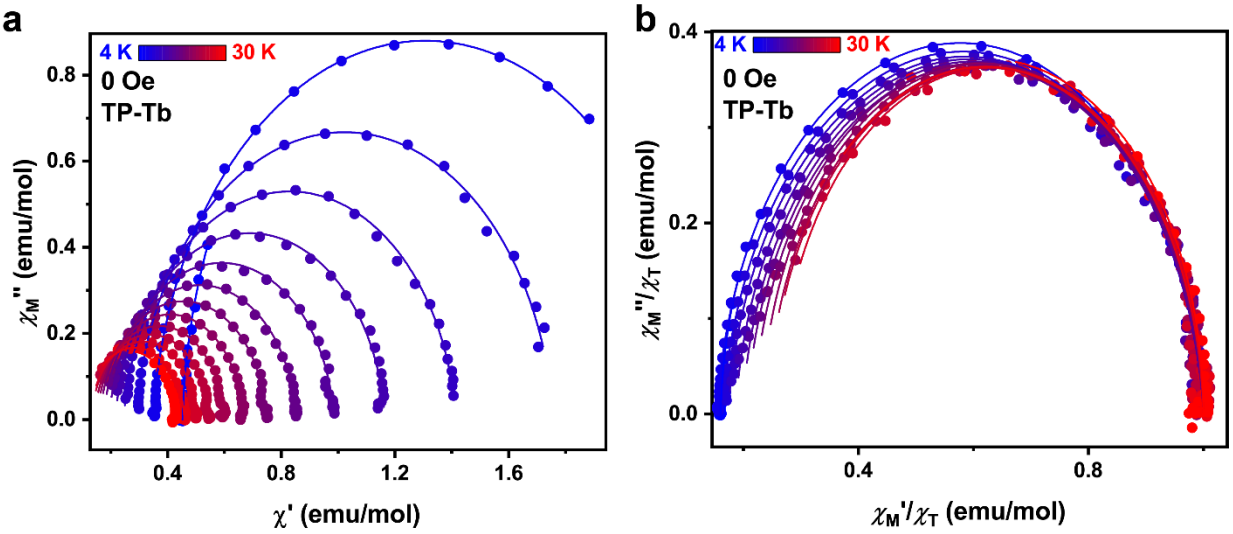

Figure S11. (a) Cole-Cole plots for **TP-Tb** from 4 K to 30 K (2 K steps). (b) Normalized Cole-Cole plots for **TP-Tb** from 4 K to 30 K (2 K steps) (normalized by χ_T which is the isothermal susceptibility). The lines represent fits to the data using a generalized Debye model, which were used to extract τ values at each temperature.

Generalized Debye model:

$$\chi(\omega) = \chi_S + \frac{\chi_T - \chi_S}{1 + (i\omega\tau)^{1-\alpha}}$$

Table S11. Cole-Cole fitting parameters for one relaxation process in **TP-Tb** under zero magnetic field from 4 K to 30 K.

Temperature	χ_S	χ_T	α	τ
4	0.45283	2.82545	0.02493	5.85717
5	0.39555	2.56448	0.03632	1.3348
6	0.34896	2.26369	0.0539	0.44409
7	0.31544	1.99555	0.06256	0.19639
8	0.28817	1.75753	0.06131	0.10427
9	0.26704	1.57932	0.06079	0.06464
10	0.24529	1.41478	0.06292	0.04401
11	0.23308	1.27664	0.05425	0.03244
12	0.2167	1.16456	0.05779	0.02519
13	0.20425	1.06887	0.05578	0.02032
14	0.19505	0.9852	0.05263	0.01704
15	0.18308	0.91552	0.05455	0.01449
16	0.17552	0.85312	0.05221	0.01272
17	0.17208	0.79163	0.03748	0.01133
18	0.16284	0.74721	0.03941	0.01011
19	0.15787	0.70345	0.03503	0.0092
20	0.15379	0.66467	0.02936	0.00848
21	0.14758	0.6304	0.03735	0.00791
22	0.14435	0.59597	0.0246	0.00721
23	0.13547	0.56901	0.02548	0.0066
24	0.13373	0.54422	0.02486	0.00606
25	0.1278	0.51905	0.02408	0.00531
26	0.12975	0.49885	0.01275	0.00451
27	0.11742	0.47932	0.02843	0.00335
28	0.11149	0.45865	0.02521	0.0023
29	0.11695	0.44155	1.50E-14	0.0015
30	0.10967	0.42643	2.76E-15	8.85E-04

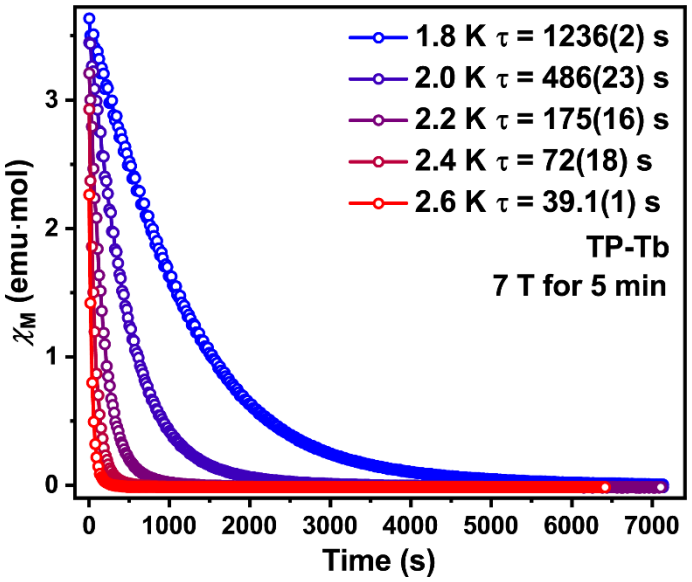

Figure S12. Dc magnetic relaxation data for the solid sample of **TP-Tb** collected at 1.8 K, 2.0 K, 2.2 K, 2.4 K and 2.6 K under zero field after magnetization at 7 T for 5 minutes. The solid lines represent the fit to the data using stretched exponential functions, $M(t) = M_1 + (M_0 - M_1)^{(\frac{t}{\tau})^n}$.

Table S12. Parameters used to fit dc magnetic relaxation data for **TP-Tb** and magnetic relaxation times extracted from these fits.

Temperature	τ	n	M_0	M_1
1.8	1235.672	1.14383	3.56124	0.01718
2	485.9932	1.03271	3.57313	-0.00339
2.2	174.6286	0.97292	3.41014	-0.01141
2.4	72.09122	0.88721	3.19165	-0.01331
2.6	39.09675	0.92156	2.26816	-0.01377

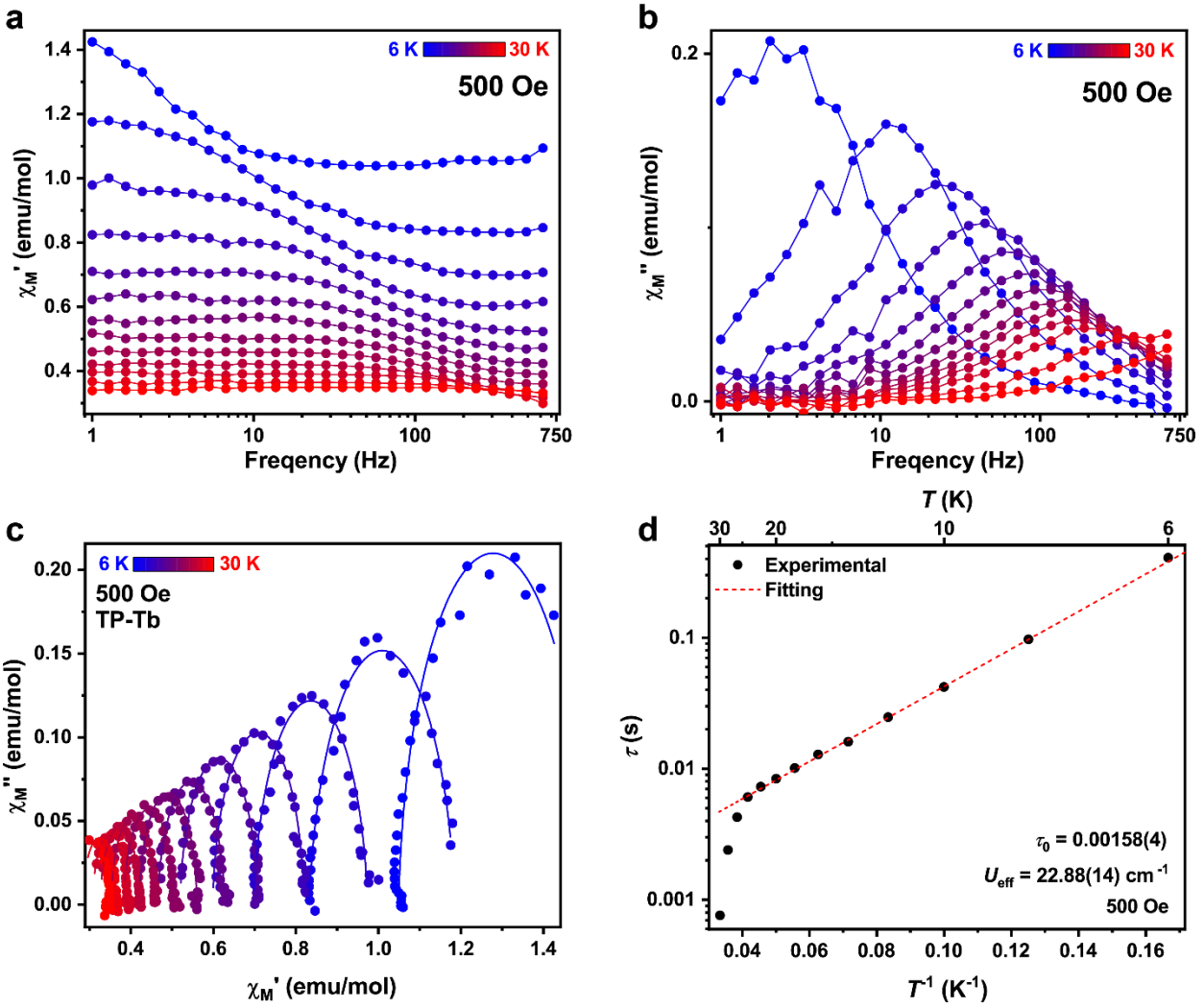

Figure S13. (a) Frequency dependence of χ_M' under 500 Oe dc magnetic field from 6 K to 30 K for **TP-Tb**. (b) Frequency dependence of χ_M'' under 500 Oe dc magnetic field from 6 K to 30 K for **TP-Tb**. The lines are shown to guide the eye in (a) and (b). (c) Cole-Cole plots for **TP-Tb** from 6 K to 30 K (2 K steps) under 500 Oe dc magnetic field. The lines represent fits to the data using a generalized Debye model, which were used to extract τ values at each temperature. (d) Inverse temperature dependence of relaxation time, τ for **TP-Tb** from 6 K to 30 K under 500 Oe. The red dashed line correspond to the fits of τ from 6 K to 22 K to the function $\tau^{-1} = \tau_0^{-1} \exp(-U_{eff} / k_B T)$.

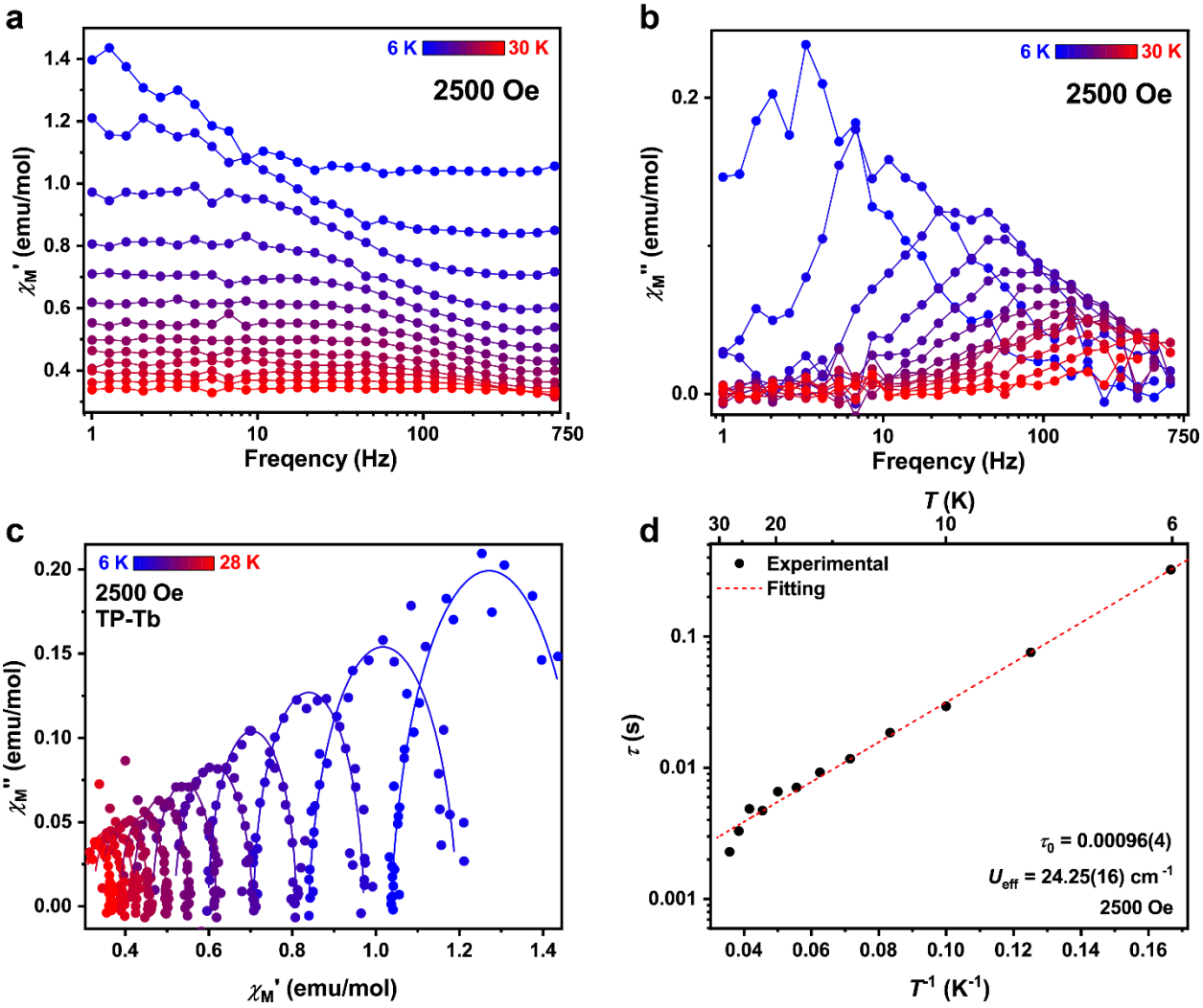

Figure S14. (a) Frequency dependence of χ_M' under 2500 Oe dc magnetic field from 6 K to 30 K for **TP-Tb**. (b) Frequency dependence of χ_M'' under 2500 Oe dc magnetic field from 6 K to 30 K for **TP-Tb**. The lines are shown to guide the eye in (a) and (b) (c) Cole-Cole plots for **TP-Tb** from 6 K to 28 K (2 K steps) under 2500 Oe dc magnetic field. The lines represent fits to the data using a generalized Debye model, which were used to extract τ values at each temperature. (d) Inverse temperature dependence of relaxation time, τ for **TP-Tb** from 6 K to 28 K under 2500 Oe. The red dashed line correspond to the fits of τ from 6 K to 22 K to the function $\tau^{-1} = \tau_0^{-1} \exp(-U_{eff} / k_B T)$.

Table S13. Cole-Cole fitting parameters for one relaxation process in **TP-Tb** under 500 Oe magnetic field from 6 K to 30 K.

Temperature	χ_S	χ_T	α	τ
6	1.04903	1.507	0.05532	0.40804
8	0.83254	1.18562	0.09588	0.09713
10	0.69791	0.97385	0.07939	0.04209
12	0.59877	0.81984	0.04661	0.02477

14	0.51933	0.70826	0.04856	0.01614
16	0.46531	0.62746	0.06233	0.01284
18	0.42027	0.56005	0.02958	0.01015
20	0.38331	0.50498	0.0399	0.0084
22	0.35275	0.45913	0.00941	0.0073
24	0.32641	0.42094	0.01005	0.00609
26	0.3079	0.39267	1.91E-15	0.00429
28	0.28434	0.3641	6.90E-16	0.00241
30	0.26443	0.34626	2.11E-15	7.64E-04

Table S14. Cole-Cole fitting parameters for one relaxation process in **TP-Tb** under 2500 Oe magnetic field from 6 K to 28 K.

Temperature	χ_S	χ_T	α	τ
6	1.03639	1.50593	0.10389	0.32279
8	0.83929	1.19496	0.09126	0.07587
10	0.70749	0.97082	0.02289	0.02941
12	0.59974	0.80887	0.00344	0.01853
14	0.51722	0.70524	0.07455	0.01172
16	0.46502	0.61823	0.03145	0.00922
18	0.41697	0.55206	0.03802	0.00706
20	0.38699	0.49977	0.03272	0.00658
22	0.33556	0.45918	0.1299	0.00471
24	0.3216	0.42412	0.07418	0.00486
26	0.30253	0.39203	0.02356	0.00329
28	0.29527	0.36613	5.54E-15	0.00229

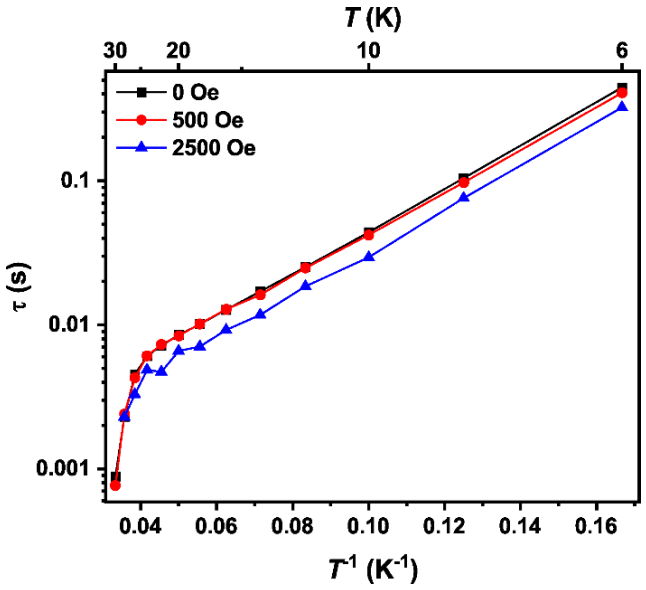

Figure S15. Inverse temperature dependence of relaxation time, τ for **TP-Tb** from 6 K to 30 K under 0 Oe (black symbols), 500 Oe (red symbols), and 2500 Oe (blue symbols).

Magnetic properties of O-Tb

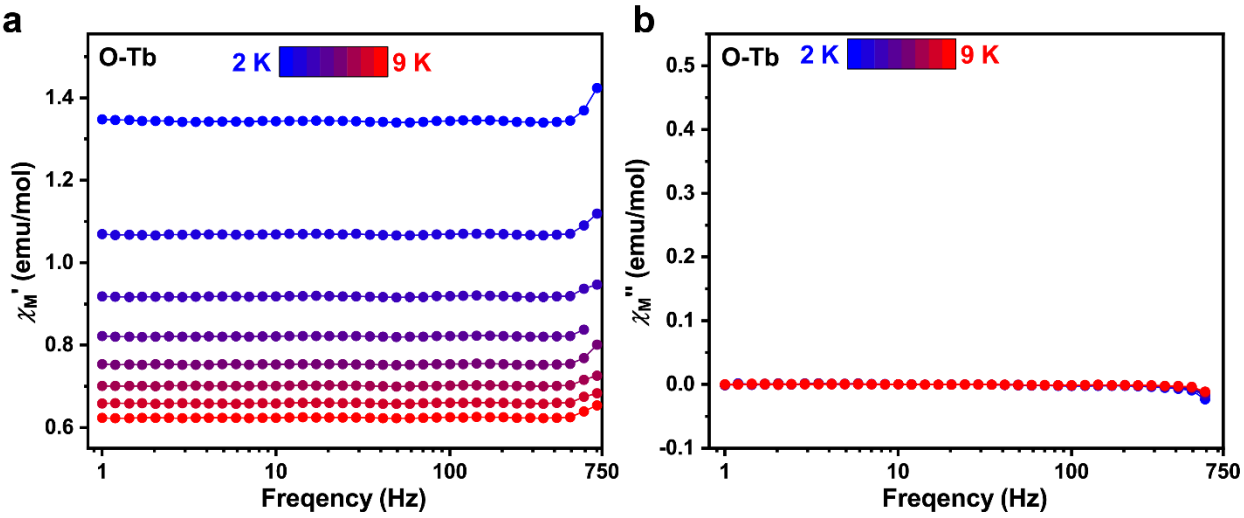

Figure S16. Frequency dependence of (a) χ_M' and (b) χ_M'' under zero dc magnetic field from 2 K to 9 K for **O-Tb**. The lines are shown to guide the eye.

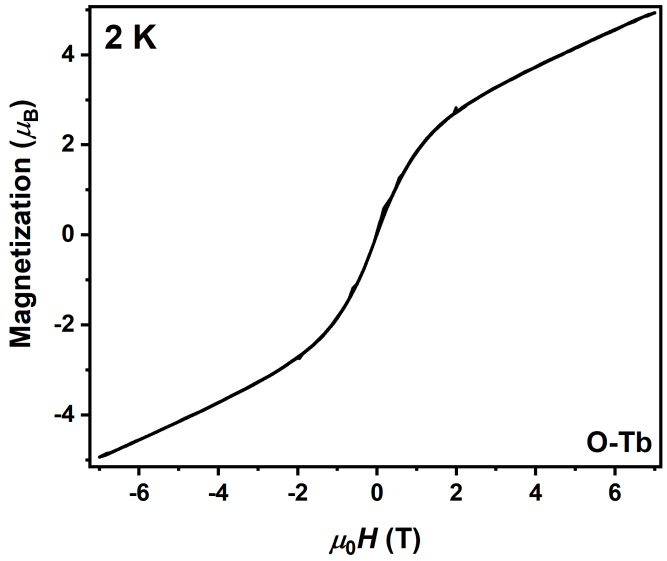

Figure S17. Magnetic field dependence of magnetization of **O-Tb** at 2 K from -7 T to 7 T.

No hysteresis loop can be observed in Fig. S16 which confirms the absence of slow relaxation in **O-Tb** at 2 K.

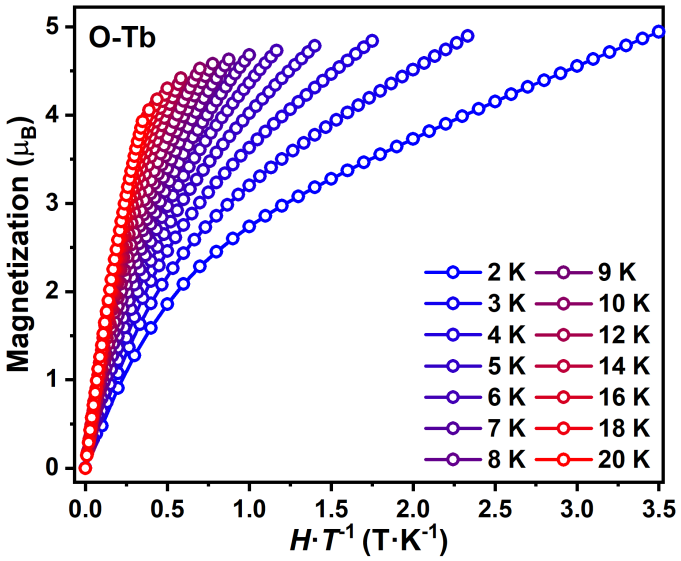

Figure S18. H/T dependence of magnetization for **O-Tb** from 2 K to 20 K. The lines are shown to guide the eye.

Magnetic properties of TP-Gd

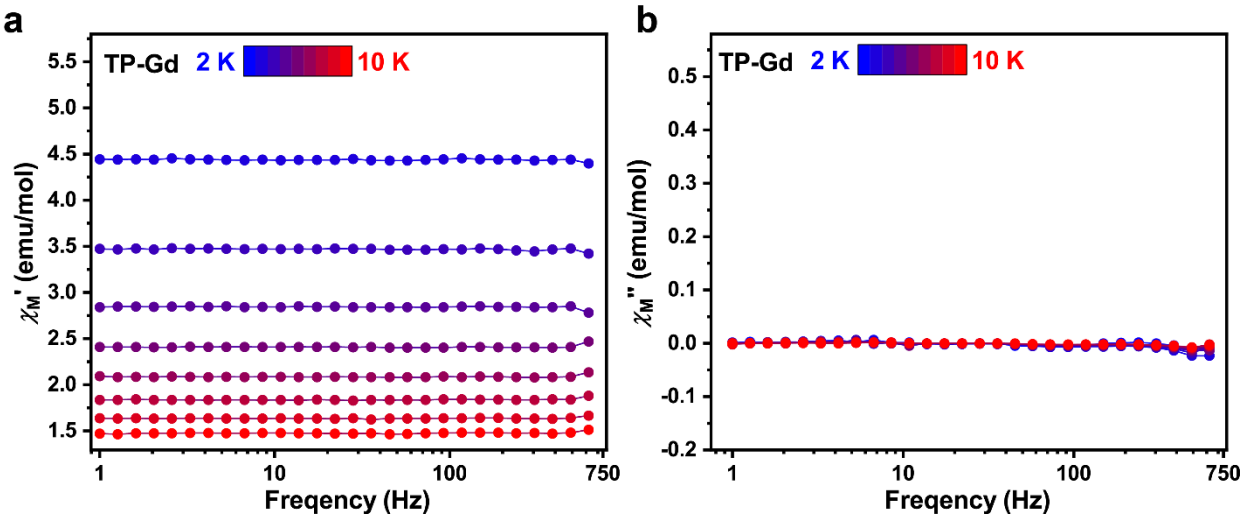

Figure S19. Frequency dependence of (a) χ_M' and (b) χ_M'' under zero dc magnetic field from 2 K to 10 K for **TP-Gd**. The lines are shown to guide the eye.

The negligible χ_M'' value for **TP-Gd** from 2 K to 10 K indicates the lack of slow magnetic relaxation behavior for **TP-Gd** in the probed temperature range.

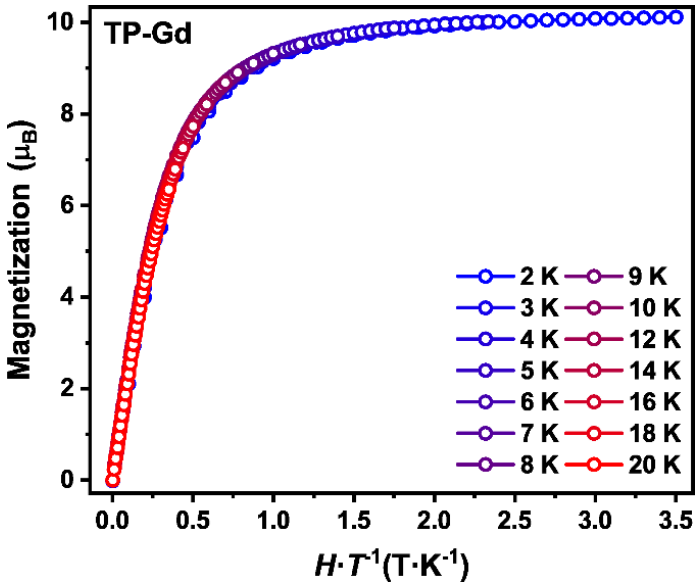

Figure S20. H/T dependence of magnetization for **TP-Gd** from 2 K to 20 K. The lines are shown to guide the eye.

The superposition of the H/T dependence of magnetization curves at different temperature suggests the lack of single-ion anisotropy for Gd^{3+} in **TP-Gd**.

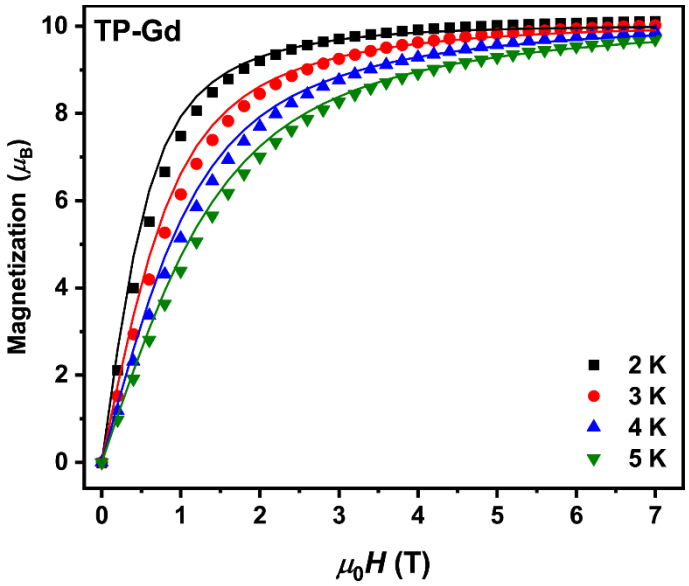

Figure S21. Magnetic field dependence of magnetization for **TP-Gd** from 2 K to 5 K. The solid lines are fitting results to the magnetic field dependence of magnetization. Details of fitting are described in the previous section.

Magnetic relaxation time fitting.

Fitting data from 1.8 K to 30 K with different models consists of multiple relaxation pathways were attempted. Several models were used.

(1) Two Orbach process, $\tau^{-1} = \tau_{0,1}^{-1} \exp(-U_{eff} / k_B T) + \tau_{0,2}^{-1} \exp(-U_{eff} / k_B T)$;

The fitting results are good as shown in the main text with R^2 value > 0.9999.

(2) Two Orbach process, one QTM process, $\tau^{-1} = \tau_{0,1}^{-1} \exp(-U_{eff} / k_B T) + \tau_{0,2}^{-1} \exp(-U_{eff} / k_B T) + \tau_{QTM}^{-1}$).

Although the fitting results lead to R^2 value > 0.9999, the τ_{QTM} value is extremely large despite the fitting range ($\tau_{QTM} > 10^{10}$ s) which agrees with the conclusion of a long QTM process in **TP-Tb**.

(3) one Orbach process and one Raman process, $\tau^{-1} = \tau_0^{-1} \exp(-U_{eff} / k_B T) + cT^n$;

The best fitting results has R^2 value > 0.9999.

However, as shown in Figure S22, this fitting results can not describe the high temperature data (20 K to 30 K) well.

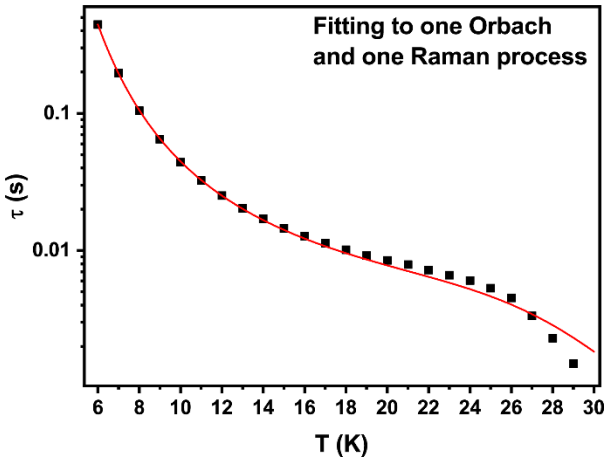

Figure S22. Temperature dependence of τ of **TP-Tb**. The red line corresponds to the fits of τ from 8 K to 30 K to the function $\tau^{-1} = \tau_0^{-1} \exp(-U_{eff} / k_B T) + cT^n$.

Table S15. Comparison of the magnetic relaxation behavior of **TP-Tb** with reported *f*-element based SMMs.

Complexes	U_{eff} / cm^{-1}	τ_0 / s	T_H [a] / K	**Reference**
TP-Tb	23.97(5)	0.00152(2)	3	**This work**
$[TbPc_2][TBA]$	230	6.3×10^{-8}		[10]
$TbPc_2$	410	1.5×10^{-9}	2	[11]
$[K(18\text{-}C\text{-}6)][((Me_3Si)_2N)_2(THF)Dy]_2(N_2)$	123	8.0×10^{-9}	8	[12]
$[K(crypt\text{-}222)][Cp^{Me4H}{}_2Tb]_2(\mu\text{-}N_2)$	276	1.3×10^{-7}	30	[13]
$[Dy(C_5H_2{}^tBu_3\text{-}1,2,3)_2][B(C_6F_5)_4]$	1223	2.0×10^{-11}	60	[14]
$[(\eta^5\text{-}Cp^*)Dy(\eta^5\text{-}Cp^{iPr5})]\ [B(C_6F_5)_4]$	1541	4.2×10^{-12}	80	[15]
$[K(18\text{-crown-}6)(THF)_2][Er(COT)_2]$	150	6.9×10^{-8}	10	[16]
$[Er_2(COT'')_3]$	219	5.0×10^{-9}	12	[17]
$[Li_2Cl(THF)_6][Dy3Fc_6Li_2(THF)_2]$	237	2.34×10^{-8}	5	[18]
$Dy(Cy_3PO)_2(H_2O)_5]Br_3{\cdot}2(Cy_3PO){\cdot}2H_2O{\cdot}2EtOH$	543	2.0×10^{-11}	20	[19]
$(Cp^{iPr5})_2Dy_2I_3$	1631	$10^{-12.2(3)}$	72	[20]

a. T_H is the temperature when magnetic hysteresis closes.

6. Computational methods and details

The electronic structure calculations were performed with the OpenMolcas software package.[21] To reduce the computational cost, small models of **TP-Tb** and **O-Tb** complexes were created by removing the Cp_2Ti moieties from the X-ray structures of the complexes. The reference wavefunctions were obtained using the state-averaged complete active space self-consistent field [SA(7)-CASSCF(8,7)] calculations, with the active space comprising of eight electrons distributed over seven *f*-orbitals. The state averaging was performed over the seven states arising from the orbital angular momentum degeneracy of the $^7F_6$ level of Tb^{3+}. The multi-state complete active space second-order perturbation theory (XMS-CASPT2) was used to account for dynamic electron correlation. The restricted active space state interaction (RASSI) method was used to calculate the spin-orbit coupling. All calculations were performed using the ANO-RCC basis set with triple-zeta contraction on Tb and double-zeta contraction on Cl atoms. The magnetic properties were obtained with the SINGLE_ANISO program.[22] The transition magnetic dipole moments between the states *i* and *j* (in the units of Bohr magneton, μ_B) were calculated by averaging over the x, y, and z components as:

$$\mu_{ij} = \frac{1}{3}\left(|\langle i|\mu_x|j\rangle| + |\langle i|\mu_y|j\rangle| + |\langle i|\mu_z|j\rangle|\right).$$

Table S16. Contributions (%) of the M_J components to the electronic states (S1-S13) of the O-Tb model complex.

M_J	S1	S2	S3	S4	S5	S6	S7	S8	S9	S10	S11	S12	S13
-6	30.6	36.3	0.2	0.3	9.1	0.8	5.1	1.1	7.5	3.9	0.7	1.4	2.9
-5	0.3	0.2	20.8	30.5	0.8	9.8	0.7	15	5.4	0.2	4.8	8.8	2.6
-4	14.5	12.8	0.2	0.2	1.5	8	5.3	2.4	22.3	17	3.4	6	13.8
-3	0	0	18.8	17.7	0.5	2.4	0.4	7.9	7.2	0.1	13.5	23.3	8.3
-2	1.9	0.6	0.3	0.9	22.5	2	29.3	1.3	4	6.8	5.7	3.6	21
-1	0.1	0	9.6	0	4.1	30.5	3.5	22.1	0.6	0.8	20.9	6.8	1
0	5.2	0	0.3	0.7	23.3	7.5	11.4	0.5	5.8	42.8	1.6	0	0.9
+1	0.1	0	9.6	0	4.1	30.5	3.5	22.1	0.6	0.8	20.9	6.8	1
+2	1.9	0.6	0.3	0.9	22.5	2	29.3	1.3	4	6.8	5.7	3.6	21
+3	0	0	18.8	17.7	0.5	2.4	0.4	7.9	7.2	0.1	13.5	23.3	8.3
+4	14.5	12.8	0.2	0.2	1.5	0.8	5.3	2.4	22.3	17	3.4	6	13.8
+5	0.3	0.2	20.8	30.5	0.8	9.8	0.7	15	5.4	0.2	4.8	8.8	2.6
+6	30.6	36.3	0.2	0.3	9.1	0.8	5.1	1.1	7.5	3.9	0.7	1.4	2.9

Table S17. Contributions (%) of the M_J components to the electronic states (S1-S13) of the TP-Tb model complex.

M_J	S1	S2	S3	S4	S5	S6	S7	S8	S9	S10	S11	S12	S13
-6	50	50	0	0	0	0	0	0	0	0	0	0	0
-5	0	0	50	50	0	0	0	0	0	0	0	0	0
-4	0	0	0	0	49.8	49.9	0	0.1	0	0	0	0.1	0.1
-3	0	0	0	0	0	0	43.2	0	15.6	6.8	34.4	0	0
-2	0	0	0	0	0.1	0.1	0	0	0	0	0	49.9	49.9
-1	0	0	0	0	0	0	6.8	0	34.4	43.2	15.6	0	0
0	0	0	0	0	0.2	0	0	99.7	0	0	0	0	0
+1	0	0	0	0	0	0	6.8	0	34.4	43.2	15.6	0	0
+2	0	0	0	0	0.1	0.1	0	0	0	0	0	49.9	49.9
+3	0	0	0	0	0	0	43.2	0	15.6	6.8	34.4	0	0
+4	0	0	0	0	49.8	49.9	0	0.1	0	0	0	0.1	0.1
+5	0	0	50	50	0	0	0	0	0	0	0	0	0
+6	50	50	0	0	0	0	0	0	0	0	0	0	0

7. References

1. Coutts, R.; Wailes, P.; Martin, R., Dimeric dicyclopentadienyltitanium(III) halides. *J. Organomet. Chem.* **1973,** *47* (2), 375-382.
2. Sheldrick, G. M., SHELXT: Integrating space group determination and structure solution. *Acta Crystallogr., Sect. A: Found. Adv* **2014,** *70*, C1437.
3. Sheldrick, G. M., Crystal structure refinement with SHELXL. *Acta Crystallogr. C* **2015,** *71* (1), 3-8.
4. Pinsky, M.; Avnir, D., Continuous symmetry measures. 5. The classical polyhedra. *Inorg. Chem.* **1998,** *37* (21), 5575-5582.
5. Casanova, D.; Cirera, J.; Llunell, M.; Alemany, P.; Avnir, D.; Alvarez, S., Minimal distortion pathways in polyhedral rearrangements. *J. Am. Chem. Soc.* **2004,** *126* (6), 1755-1763.
6. Cirera, J.; Ruiz, E.; Alvarez, S., Shape and Spin State in Four-Coordinate Transition-Metal Complexes: The Case of the d^6 Configuration. *Chem. Eur. J.* **2006,** *12* (11), 3162-3167.
7. Shamir, J.; Hake, D.; Urland, W., Raman spectra of LnAl3Cl12 compounds. *J. Raman Spectrosc.* **1992,** *23* (3), 137-139.
8. Bain, G. A.; Berry, J. F., Diamagnetic corrections and Pascal's constants. *J. Chem. Educ.* **2008,** *85* (4), 532.
9. Chilton, N. F.; Anderson, R. P.; Turner, L. D.; Soncini, A.; Murray, K. S., PHI: A powerful new program for the analysis of anisotropic monomeric and exchange-coupled polynuclear d-and f-block complexes. *J. Comput. Chem.* **2013,** *34* (13), 1164-1175.
10. Ishikawa, N.; Sugita, M.; Ishikawa, T.; Koshihara, S.-y.; Kaizu, Y., Lanthanide double-decker complexes functioning as magnets at the single-molecular level. *J. Am. Chem. Soc.* **2003,** *125* (29), 8694-8695.
11. Ganivet, C. R.; Ballesteros, B.; de la Torre, G.; Clemente-Juan, J. M.; Coronado, E.; Torres, T., Influence of peripheral substitution on the magnetic behavior of single-ion magnets based on homo-and heteroleptic TbIII bis (phthalocyaninate). *Chem. Eur. J.* **2013,** *19* (4), 1457-1465.
12. Rinehart, J. D.; Fang, M.; Evans, W. J.; Long, J. R., Strong exchange and magnetic blocking in N_2^{3-}-radical-bridged lanthanide complexes. *Nat. Chem.* **2011,** *3* (7), 538-542.
13. Demir, S.; Gonzalez, M. I.; Darago, L. E.; Evans, W. J.; Long, J. R., Giant coercivity and high magnetic blocking temperatures for N_2^{3-} radical-bridged dilanthanide complexes upon ligand dissociation. *Nat. Commun.* **2017,** *8* (1), 1-9.
14. Goodwin, C. A.; Ortu, F.; Reta, D.; Chilton, N. F.; Mills, D. P., Molecular magnetic hysteresis at 60 kelvin in dysprosocenium. *Nature* **2017,** *548* (7668), 439-442.
15. Guo, F.-S.; Day, B. M.; Chen, Y.-C.; Tong, M.-L.; Mansikkamäki, A.; Layfield, R. A., Magnetic hysteresis up to 80 kelvin in a dysprosium metallocene single-molecule magnet. *Science* **2018,** *362* (6421), 1400-1403.
16. Meihaus, K. R.; Long, J. R., Magnetic blocking at 10 K and a dipolar-mediated avalanche in salts of the bis (η8-cyclooctatetraenide) complex [Er (COT) 2]−. *J. Am. Chem. Soc.* **2013,** *135* (47), 17952-17957.
17. Le Roy, J. J.; Ungur, L.; Korobkov, I.; Chibotaru, L. F.; Murugesu, M., Coupling strategies to enhance single-molecule magnet properties of erbium–cyclooctatetraenyl complexes. *J. Am. Chem. Soc.* **2014,** *136* (22), 8003-8010.
18. Latendresse, T. P.; Bhuvanesh, N. S.; Nippe, M., Hard single-molecule magnet behavior by a linear trinuclear lanthanide–[1] metallocenophane complex. *J. Am. Chem. Soc.* **2017,** *139* (42), 14877-14880.
19. Chen, Y.-C.; Liu, J.-L.; Ungur, L.; Liu, J.; Li, Q.-W.; Wang, L.-F.; Ni, Z.-P.; Chibotaru, L. F.; Chen, X.-M.; Tong, M.-L., Symmetry-supported magnetic blocking at 20 K in pentagonal bipyramidal Dy (III) single-ion magnets. *J. Am. Chem. Soc.* **2016,** *138* (8), 2829-2837.

20. Gould, C. A.; McClain, K. R.; Reta, D.; Kragskow, J. G.; Marchiori, D. A.; Lachman, E.; Choi, E.-S.; Analytis, J. G.; Britt, R. D.; Chilton, N. F., Ultrahard magnetism from mixed-valence dilanthanide complexes with metal-metal bonding. *Science* **2022,** *375* (6577), 198-202.
21. Fdez. Galván, I.; Vacher, M.; Alavi, A.; Angeli, C.; Aquilante, F.; Autschbach, J.; Bao, J. J.; Bokarev, S. I.; Bogdanov, N. A.; Carlson, R. K., OpenMolcas: From source code to insight. *J. Chem. Theory Comput.* **2019,** *15* (11), 5925-5964.
22. Chibotaru, L. F.; Ungur, L., Ab initio calculation of anisotropic magnetic properties of complexes. I. Unique definition of pseudospin Hamiltonians and their derivation. *Chem. Phys.* **2012,** *137* (6), 064112.